

Research Article

Characterization and Evaluation of Zeolite A/Fe₃O₄ Nanocomposite as a Potential Adsorbent for Removal of Organic Molecules from Wastewater

Emmanuel Nyankson, Jonas Adjasoo, Johnson Kwame Efavi , Reuben Amedalor, Abu Yaya , Gloria Pokuaa Manu, Kingsford Asare, and Nii Amarkai Amartey

University of Ghana, School of Engineering Sciences, Department of Materials Science & Engineering, P.O. BOX LG 74, Accra, Ghana

Correspondence should be addressed to Johnson Kwame Efavi; jkefavi@ug.edu.gh

Received 22 March 2019; Revised 3 July 2019; Accepted 28 July 2019; Published 27 August 2019

Academic Editor: Luqman C. Abdullah

Copyright © 2019 Emmanuel Nyankson et al. This is an open access article distributed under the Creative Commons Attribution License, which permits unrestricted use, distribution, and reproduction in any medium, provided the original work is properly cited.

In this work, zeolite (Z) and Z-Fe₃O₄ nanocomposite (Z-Fe₃O₄ NC) have been synthesized. The Fe₃O₄ nanoparticles were synthesized using the extract from maize leaves and ferric and ferrous chloride salts and encapsulated into the zeolite framework. The nanocomposite (Z-Fe₃O₄ NC) was characterized using X-ray diffractometer (XRD), Fourier-transform infrared (FT-IR) spectroscopy, energy-dispersive X-ray (EDX) spectroscopy, and scanning electron microscopy (SEM). The potential of Z-Fe₃O₄ NC as an adsorbent for removing methylene blue molecules (MB) from solution was examined using UV-Vis and kinetic and equilibrium isotherm models. The adsorption data fitted best with the pseudo-second-order model and Weber and Morris model, indicating that the adsorption process was chemisorption, while the Weber and Morris described the rate-controlling steps. The intraparticle diffusion model suggests that the adsorption processes were pore and surface diffusion controlled. The Langmuir isotherm model best describes the adsorption process indicating homogeneous monolayer coverage of MB molecules onto the surface of the Z-Fe₃O₄ NC. The maximum Langmuir adsorption capacity was 2.57 mg/g at 25°C. The maximum adsorption efficiency was 97.5%. After regeneration, the maximum adsorption efficiency achieved at a pH of 7 was 82.6%.

1. Introduction

Clean water is an essential element for the survival of all living organisms. However, due to the rapid pace of industrialization in the textile, food, and plastics sector, these industries discharge wastewater containing “dye pollutants” into water bodies as production byproducts. These pollutants have a serious effect on aquatic living organisms and the general environment [1, 2].

In the past, technologies such as solvent extraction, sedimentation, coagulation, oxidation, adsorption, evaporation, distillation, reverse osmosis, ion exchange, and electrolysis were developed for treating wastewater. Among these techniques, adsorption is an excellent method capable

of removing organic molecules through the use of an adsorbent media.

Characteristically, an ideal adsorbent must possess high surface area, good physical, mechanical, and chemical stability, and high affinity to bind with pollutant molecules [1–3]. Also, an effective adsorption process depends on several factors such as pH and temperature, the structure and concentration of the adsorbate, degree of ionization of the adsorbate, the ionic strength of dispersion, and the structure and surface charge of the adsorbent [4].

Recently, nanoscience and nanotechnology have emerged with the synthesis of nanocomposite adsorbents with excellent catalytic adsorption characteristics. Nano-adsorbents possess small size, a large surface area to volume

ratio, and high reactivity and catalytic potential caused by the size quantization effect [5]. During adsorption, they provide fast kinetics and sorption capacity with extremely high pollutant-binding affinity associated with their sorption sites with regeneration effects [3, 5, 6].

Metal oxide nanoparticles (MONs), such as MnO, Al₂O₃, TiO₂, and CeO₂, have shown to have excellent kinetics for pollutant removal from aqueous systems [7–10]. In the nanoregime, their surface energy increases, causing poor stability, and they are prone to agglomeration with loss of adsorption capacity and selectivity [11–14]. When these MONs are impregnated into porous support systems, their capacity improves tremendously [15–18].

Iron oxide nanocomposite has shown a tremendous promise in a number of environmental remediation effects due to their superparamagnetic property. Promising among them, nanomagnetite (Fe₃O₄) particles have high chemical stability, high coercivity, low Curie temperature, and low toxicity and are biocompatible [19–22].

Several synthesis methods such as the microemulsion technique, hydrolysis, hydrothermal method, sol-gel process, and coprecipitation synthesis exist for synthesizing magnetic magnetite. Coprecipitation has been an efficient and effective method, but it is an expensive chemical method which produces large nanoparticle sizes within a short time accompanied with residual chemicals in the composite which may have a detrimental effect on the environment and the human health upon application in water treatment [23–27]. In order to further improve the nanoparticles' stability, improve the number of active sites, and decrease the agglomeration of the magnetite nanoparticles, an effective approach has been developed to fabricate composite adsorbents by impregnating or coating the Fe₃O₄ particles into/onto porous supports such as zeolite and to provide a higher excellent mechanical stability with large surface area to enhance their adsorption capacity [15–18].

Currently, there is much interest in the biological synthesis using biological materials and organisms such as algae, bacteria, yeast, fungi, and plants [27]. To prevent the accumulation and to increase the stability of the Fe₃O₄ nanoparticles, strong biomolecule stabilization agents are used which are naturally produced or found in the biological resources [27–29]. Plant extracts contain phytochemicals and biomolecules which acts as reducing agents capable of reducing metal ions or inorganic iron salts [30].

Zeolite, an aluminosilicate material, has well-defined molecular-sized pores [31]. Their frameworks are built by [SiO₄]⁴⁻ and [AlO₄]⁵⁻ tetrahedral, linked together to form cages connected by pore openings of defined size. The presence of [AlO₄]⁻ in the zeolite framework introduces negative charges which is balanced by cations such as Ca²⁺, K⁺, and Na⁺. These cations are exchangeable in solution through ionic exchange [31, 32]. Research has shown that the porous framework of zeolite has good adsorption efficiency in the removal of heavy metals like arsenic, mercury, fluoride, and organic dyes and as a host material in catalytic applications [4, 5, 16, 33].

In this work, green synthesis has been employed to synthesize magnetite nanocomposite in a zeolite framework

using the maize leaves extract as reducing and stabilizing agents which provide an efficient host medium. The as-synthesized Z-Fe₃O₄ NC was characterized using XRD, FT-IR, EDX, and SEM to confirm the formation of zeolite-magnetite nanocomposite (Z-Fe₃O₄ NC). Their adsorption capacities for MB organic molecules were investigated using UV-Vis, kinetics, and isotherm models.

2. Materials and Methods

2.1. Materials. The analytical graded chemicals were used without purification.

Sodium hydroxide (NaOH, 99%), hydrochloric acid (HCl, 99%), iron (II) chloride tetrahydrate (FeCl₂·4H₂O, 99%), iron (III) chloride hexahydrate (FeCl₃·6H₂O, 98%), and methylene blue (MB) were obtained from Sigma Aldrich, United Kingdom (UK). In addition, kaolin, a natural aluminosilicate-based deposit was sampled from Saltpond, in the Central Region of Ghana which served as the raw material for the synthesis of zeolite.

MB was used as a dye pollutant. MB is a cationic dye made of heterocyclic aromatic chemical compounds with a molecular weight of 373.9 g/mol, as shown in Figure 1. The maximum absorbance occurs at a wavelength corresponding to 664 nm [34, 35].

2.2. Synthesis of Zeolites. Particle-size analysis $\leq 75 \mu\text{m}$ was done with Retsch VS1000 mechanical shaker on the raw kaolin sample to achieve a fine particle-size distribution. The unreactive kaolin sample was calcined at 600°C to convert it into the more reactive metakaolinite phase. This was then reacted with a 2 M NaOH aqueous solution in a solid-to-liquid (S/L) ratio of 10 g/50 mL and stirred using a magnetic stirrer for 30 minutes to give a homogeneous mixture. The mixture was crystallized for 7 hours at 100°C after aging for 24 hours. The sample was filtered and washed with excess deionized water until the pH of the filtrate was around 7. This was followed by oven-drying at a temperature of 70°C. The samples were later powdered for characterization [32].

2.3. Extract from Maize Leaves. The maize leaves samples were washed and dried in an oven at 60°C for 12 hours. The dried leaves were ground into a fine powder. An amount of 10 g of dried powder was taken into 250 mL round-bottom flask, and 100 mL of distilled water was added and refluxed for 60 min at 80°C until the color of the aqueous solution changes to deep green. The resultant mixture was then cooled to room temperature and filtered with a cheesecloth and filter paper. The resultant extract was stored at -4°C.

2.4. Synthesis of Zeolites/Magnetite Nanocomposite. The magnetite nanoparticles were synthesized before their subsequent incorporation into the zeolite framework using an already established method by Izadiyan et al. [28]. 5.52 g of FeCl₃ hexahydrate and 1.98 g of FeCl₂ tetrahydrate (2.8 : 1 molar ratio) were dissolved in 200 mL of DI water. 40 mL of the maize extract was added to the

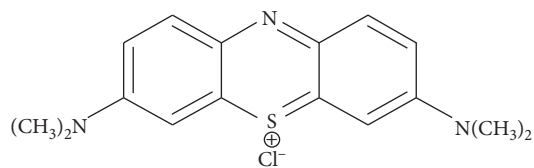


FIGURE 1: Molecular structure of methylene blue dye [34].

mixture. This stage is followed by the drop-wise addition of 2 M NaOH to the solution under continuous stirring at a pH of 11. Stirring was allowed for 1 h to ensure a homogeneous solution and to complete the reaction. The appearance of a black precipitate confirmed the formation of the magnetite nanoparticles (Fe_3O_4). The as-synthesized magnetite (Fe_3O_4) nanoparticles were separated using a permanent magnet. The formed Fe_3O_4 -NPs were washed using deionized water and dried in an oven at around 70°C overnight.

In the synthesis of the composite, 4 g of the as-synthesized zeolite was added to 100 mL of the magnetite solution followed by continuous stirring for 6 hours. The mixture was then left for 24 hours. The next step is the washing and centrifugation of the mixture to separate the zeolite/magnetite composite from the solution. The last stage of the synthesis process involved drying the sample in an oven at 60°C overnight.

2.5. X-Ray Diffraction (XRD). XRD is a powerful powder diffraction technique for phase identification of crystalline materials. Powder XRD patterns were recorded using the Empyrean PANalytical series 2 X-ray Diffractometer (XRD) with $\text{CuK}\alpha$ (1.54 \AA). 1 gram of the powder sample was compacted on a flat working surface and later transferred into a sample holder and scanned between a 2θ angular range of 0 – 100° . The phases present were identified using X'Pert Highscore plus database software.

2.6. Energy-Dispersive X-Ray (EDX) Analysis and Scanning Electron Microscopy (SEM). The structural morphology and empirical elemental compositions were estimated using energy-dispersive X-ray (EDX) spectroscopy and Zeiss EVO LS10 scanning electron microscopy (SEM) equipped with the Oxford INCA X-act detector.

2.7. Fourier-Transform Infrared (FT-IR) Spectroscopy. FT-IR spectroscopy is a technique used to determine the structure of molecules with the molecular characteristic absorption of infrared radiation capable of determining bond mechanisms. In this work, attenuated total reflectance (ATR) was employed with single bounce diamond anvil ATR accessory fitted to a Thermo-Fisher Nicolet IS50 FT-IR spectrometer. About 0.2 grams of the samples were placed on the diamond ATR plate, and measurements were taken.

2.8. UV-Vis Spectroscopy. The adsorption of the MB molecules onto the zeolite/magnetite nanocomposite adsorbent

surface was monitored using a GENESYS 10S UV-Vis spectroscopy (version v4.005 2L5S048209). Characteristic peak of MB was observed at 665 wavelength, and its absorbance was measured to estimate the corresponding concentration from a calibration curve.

2.9. Adsorption Experiments. The aim of this study is to investigate the potential of the Z- Fe_3O_4 NC as an adsorbent for adsorbing MB molecules from solution and to describe the adsorption mechanisms using kinetic and isotherm models.

The batch adsorption experiment was generally carried out using an adsorbent loading of 2.8 mg, at pH of 9 and at a room temperature of 25°C . During the experiment, 3.5 mL of 2 mg/L concentration of methylene blue (MB) aqueous solution was added to 2.8 mg of zeolite/magnetite nanocomposite in a cuvette, and the absorbance was collected over a period of 3 hours [32]. This procedure was repeated using 4, 6, 8, and 10 mg/L concentrations of MB to study the effect of dye concentration on equilibrium.

From the adsorption experiments, the adsorption capacity, q_t (mg/g) equation (1), which represents the amount of dye adsorbed per unit weight of zeolite and the dye removal efficiency, (R%) equation (2), were calculated as follows:

$$\text{adsorption capacity, } q_t = \frac{(C_0 - C_t)V}{W}, \quad (1)$$

$$\text{removal efficiency (\%), } R = \frac{(C_0 - C_t)}{C_t} \times 100, \quad (2)$$

where C_0 is the dye concentration at time $t = 0$ (mg/L), C_t is the dye concentration at time $t = t$ (mg/L), V is the volume of MB or RhB solution (mL), and W is the mass of adsorbent used (mg).

The absorbance was measured a Genesys 10S UV-Vis spectrophotometer at the MB characteristic monochromatic wavelength (λ_{max}) of 665 nm. This absorbance study was repeated using only pure zeolite without the presence of magnetite nanoparticles addition.

2.9.1. Regeneration of Spent Adsorbent. To study the regeneration ability of the Z- Fe_3O_4 NC, the spent zeolite/magnetite nanocomposites were washed in varying pH values of 5, 7, 9, 11, and 13 using 0.1 mol/L NaOH and HCl solutions and loaded using 3.5 ml of 2 mg/l MB concentration at a room temperature of 25°C . From the literature, the pH of batch formulations plays a major role in the adsorption/desorption processes by affecting the changes in the surface charge distribution of adsorbents used [36].

2.9.2. Adsorption Kinetics. The kinetic models are used to examine the various mechanisms controlling the adsorption of the dye molecules from the aqueous solution; that is, these models help to describe the solute uptake rate from the solute-solution interface. The kinetics of the adsorption process can be modeled by the pseudo-first-order Lagergren

equation, pseudo-second-order rate equation, and the intraparticle diffusion model given below [37, 38]. In this work, the pseudo-first-order (PFO) kinetic model, pseudo-second-order (PSO) kinetic model, and an intraparticle diffusion model were applied. The PFO can be modeled using Lagergren's first-order rate equation. The PFO kinetic model after integration and inserting necessary boundary conditions is given by

$$\log(q_e - q_t) = \log q_e - \frac{k_1}{2.303} t, \quad (3)$$

where q_t is the amount of adsorbate adsorbed at time t (mg/g), q_e is the adsorption capacity at equilibrium (mg/g), k_1 is the pseudo-first-order adsorption rate constant (min^{-1}), and t is the adsorption contact time (min). The PSO kinetic model states that the rate of solute uptake is directly proportional to the square of the difference in concentration between the equilibrium dye adsorption capacity and the concentration of the dye adsorbed onto the adsorbent at any time t [39]. The PSO kinetic model after integration and inserting all the necessary boundary conditions is given as follows:

$$\frac{t}{q_t} = \frac{1}{k_2 q_e^2} + \frac{t}{q_e}, \quad (4)$$

where k_2 is the pseudo-second-order rate constant ($\text{g}\cdot\text{mg}^{-1}\cdot\text{min}^{-1}$).

Again, the possibility of the adsorption mechanism being affected by the intraparticle diffusion resistance was explored using the intraparticle diffusion model. Weber and Morris in their work in 1962 posited that the analysis of this model determined the rate-controlling steps of the adsorption process. Film diffusion, pore diffusion, surface diffusion, or a combination during the adsorption phenomenon describes the intraparticle diffusion mechanism. The intraparticle diffusion is given as follows [40]:

$$q_t = k_i t^{0.5} + C_i, \quad (5)$$

where k_i is the intraparticle diffusion rate constant ($\text{mg}\cdot\text{g}^{-1}\cdot\text{min}^{-0.5}$) and C_i is the intercept which corresponds to the boundary layer thickness (mg/g). The larger the intercept is, the greater the boundary layer effect.

2.9.3. Equilibrium Adsorption Kinetics. The analysis of the adsorption equilibrium models can provide useful information regarding the sorption mechanism, surface properties, and affinity of adsorbent used [41]. Although there are several isotherm equations for analyzing the experimental sorption equilibrium parameters, the commonly used ones are the Langmuir and the Freundlich models. The Langmuir isotherm model is based on the assumption that the adsorbent surface has a finite number of active sites which are homogeneously distributed over its surface allowing a homogeneous monolayer adsorption of adsorbate. During the adsorption process, one active site adsorbs a dye molecule and after does not allow any additional adsorption at the occupied active site [42–44]. The saturated monolayer isotherm model can be expressed as

$$q_e = \frac{Q_m K_L C_e}{1 + K_L C_e}. \quad (6)$$

The linearized form of equation (6) becomes

$$\frac{C_e}{q_e} = \frac{1}{Q_m K_L} + \frac{C_e}{Q_m}, \quad (7)$$

where Q_m is the maximum adsorption capacity at monolayer (mg/g), K_L is the Langmuir adsorption constant (L/mg) related to the affinity of the binding sites, and C_e is the equilibrium concentration of the adsorbate.

A plot of C_e/q_e against C_e from equation (7) gives a straight line with slope $1/Q_m$ and an intercept $1/Q_m K_L$ when the experimental data fit the Langmuir isotherm model. In determining the suitability of the Langmuir model in modeling a given adsorption process, a dimensionless parameter known as the separation factor (R_L) is used [42, 43, 45]. R_L is defined as follows:

$$R_L = \frac{1}{1 + K_L C_o}, \quad (8)$$

where R_L is the separation factor (dimensionless), K_L is the Langmuir adsorption constant (L/mg), and C_o is the initial concentrations of MB (mg/L).

For an unfavorable adsorption process, $R_L > 1$, when $R_L = 0$, it indicates that the adsorption is irreversible, and for $0 < R_L < 1$, it implies that the adsorption process is favorable.

The Freundlich model, on the other hand, assumes that as the concentration of the adsorbate increases, the concentration of adsorbate on the adsorbent surface also increases and, correspondingly, the sorption energy exponentially decreases on completion of the sorption centers of the adsorbent, thus implying an adsorption onto heterogeneous surfaces with interaction between the adsorbed molecules which is not restricted to the formation of a monolayer [46]. The exponential form of the Freundlich equation is given as follows:

$$q_e = K_F C_e^{(1/n_f)}. \quad (9)$$

The linearized form of equation (9) is

$$\ln q_e = \ln K_F + \frac{1}{n_f} \ln C_e, \quad (10)$$

where K_F (mg/g) is the Freundlich constant related to the bonded energy and n_f is the heterogeneity factor. In addition, $1/n_f$ relates to the adsorption intensity inferring that a smaller value of $1/n_f$ below unity indicates a stronger bond between adsorbate and adsorbent.

3. Results and Discussion

3.1. X-Ray Diffraction (XRD). XRD analysis was done to analyze the phases present in the as-synthesized zeolite/magnetite nanocomposite (Z-Fe₃O₄ NC). The results from the XRD analyses are shown in Figure 2. The diffraction peaks for the composite recorded major zeolite peaks at 2θ peak positions of 7.3°, 10.3°, 12.5°, 16.2°, 21.8°, 24°, 26.7°, 27.2°, 30°, and 34.2° which corresponds to the (200), (220),

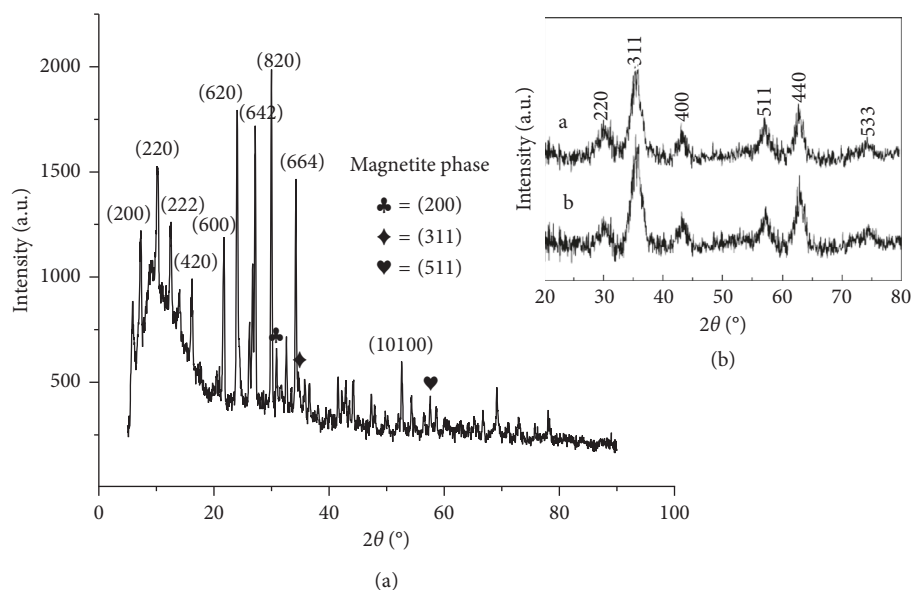


FIGURE 2: (a) XRD pattern of synthesized zeolite/magnetite nanocomposite; (b) XRD of magnetite (Fe_3O_4) [48].

(222), (420), (600), (620), (642), (820), (664), and (10100) planes, respectively, indicating that peak positions from the as-synthesized zeolite matched against that of Linde Type A [47]. Also, the magnetite phase was identified at peak positions 30.89° , 35.82° , and 57.56° corresponding to the (200), (311), and (511) planes, respectively, which confirmed the data reported by Cai et al., as shown in Figure 2(b) [48].

The crystallite size of the Z- Fe_3O_4 NC was calculated as 27.23 nm using Scherer's equation (equation (11)), at the 2θ peak position of 29.98° , a wavelength of $\lambda = 1.54178$ nm, and a shape factor of $K = 0.94$.

Scherer's equation is given as follows:

$$L = \frac{0.94\lambda}{\beta \cos \theta} \quad (11)$$

where λ is the wavelength of X-ray ($\text{CuK}\alpha$), β is the full width at half maximum, θ is the Bragg's Angle, and L is the crystallite size.

3.2. Energy-Dispersive X-Ray (EDX) Analysis. EDX was carried out to examine the elemental composition of the zeolite/magnetite nanocomposite (Z- Fe_3O_4 NC) framework. From the analysis of the data (Figure 3), it was observed that the elemental composition of the composite was as follows: O (58.89%), Al (19.34%), Si (18.18%), and Fe (3.50%). From the results, the Si/Al ratio of the as-synthesized zeolite nanocomposite was approximately 1 indicating the formation of zeolite A. Also, the presence of iron and oxygen confirmed the presence of magnetite nanoparticles in the nanocomposite.

3.3. Scanning Electron Microscopy (SEM). SEM analyses give information about the morphology and the textural properties of the as-synthesized zeolite and zeolite/magnetite nanocomposite. From Figure 4(a), the characteristic cubic

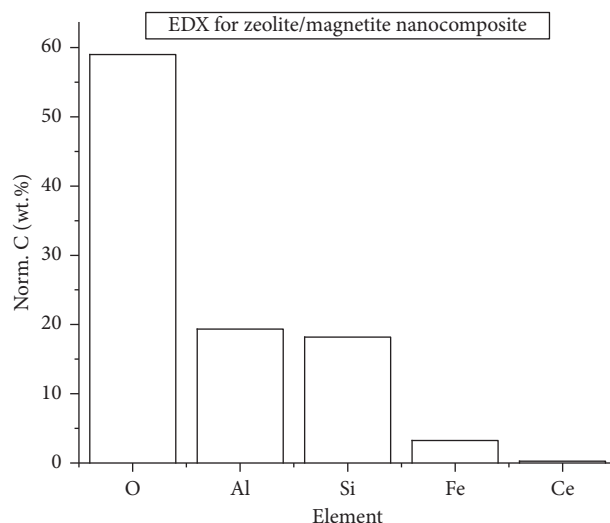


FIGURE 3: EDX of zeolite/magnetite nanocomposite.

zeolite crystals were observed which confirms the presence of the zeolite phase as already confirmed from XRD [49]. Also, the spherical morphology of the Fe_3O_4 nanoparticles, as shown in Figure 4(b), confirmed the formation of the magnetite nanoparticles as reported by Izadiyan et al. [28]. Upon the incorporation of the magnetite nanoparticles into the zeolite framework, it was observed from Figure 4(c) that there is a distortion of the original cubical structure of the zeolite. This indicates a bonding interaction between the zeolite and the Fe_3O_4 nanoparticles leading to morphological structural changes.

3.4. Fourier-Transform Infrared (FT-IR) Spectroscopy. FT-IR spectroscopy on the pure zeolite and the zeolite/magnetite nanocomposite (Z- Fe_3O_4 NC) identify the IR spectra within the range of $4000\text{--}400$ cm^{-1} and provides

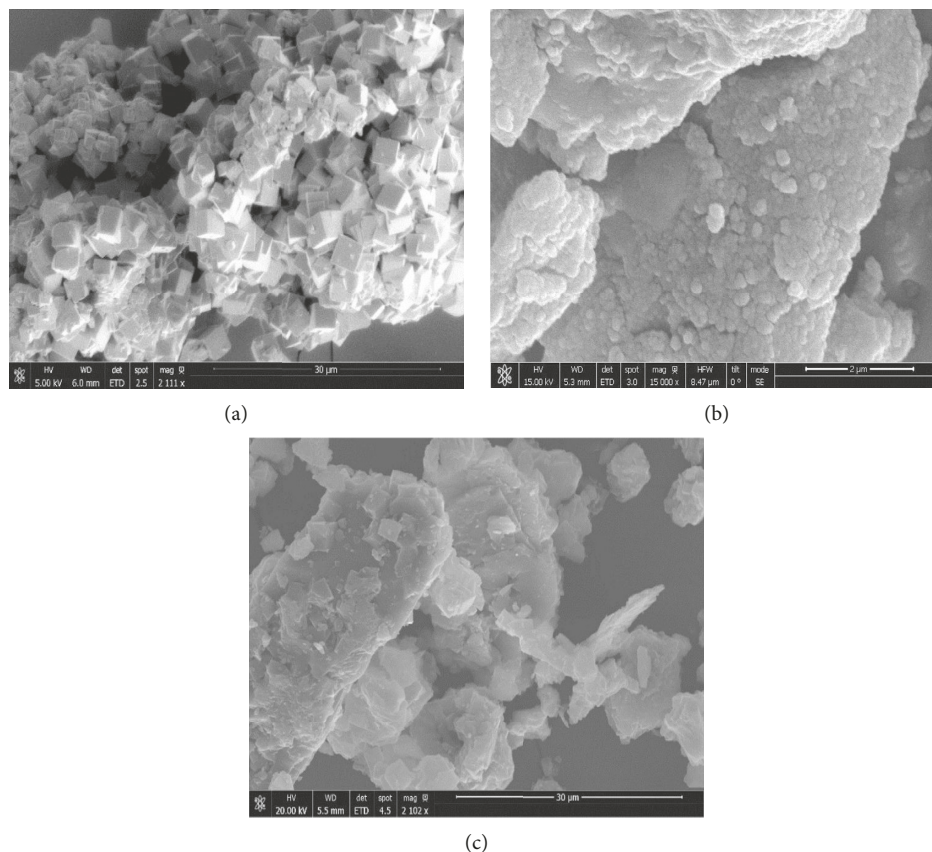


FIGURE 4: SEM of (a) pure zeolite, (b) Fe₃O₄ NP, and (c) zeolite/magnetite nanocomposite (Z-Fe₃O₄ NP).

important information corresponding to the functional groups and the vibrational bands present in their framework, as shown in Figure 5.

The spectra at position 3370 cm⁻¹ and 3339 cm⁻¹ which fall within the spectral range of 3000–3600 cm⁻¹ indicate the presence of the water of absorption that is a characteristic of the zeolite framework [50]. Similarly, the vibration stretching at 1644 cm⁻¹ and 1645 cm⁻¹ can also be attributed to the presence of coordinated hydroxyl groups on the zeolite surface [51]. The high-intensity vibration frequency at the band positions 988 cm⁻¹ and 974 cm⁻¹ found between the spectral ranges of 1250 and 950 cm⁻¹ represent the internal vibrations due to the asymmetric stretching of Si-O-Al tetrahedral. Again, the spectra 663 cm⁻¹ of the pure zeolite found between 720 and 650 cm⁻¹ can be attributed to internal vibrations due to symmetric stretching within the zeolite structure. The presence of the external T-O linkage (T = Si or Al) due to the double ring is also confirmed by the band at position 546 cm⁻¹. The band at position 462 cm⁻¹ found within the spectral range of 500–420 cm⁻¹ suggests the presence of internal tetrahedron vibrations of Si-O and Al-O of sodalite (T-O-T) with bending modes of the sodalite cages found in zeolites [52]. Moreover, Stefanovsky et al. reported that the specific vibrations of Fe-O bonds can be found around 460 cm⁻¹ and 570 cm⁻¹ [53]. From Figure 5, it was observed that 462 cm⁻¹ peak disappeared followed by a shift in the % transmittance. This observation can be attributed to the formation of the Fe-O and Fe-Al-O band [53, 54]. In

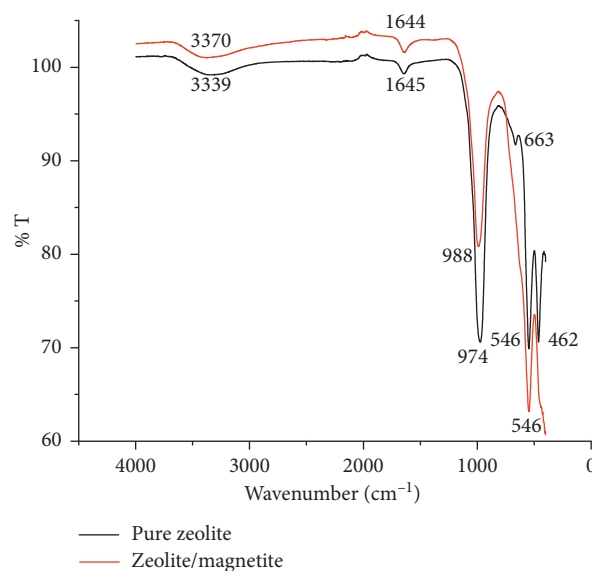


FIGURE 5: FT-IR of the pure zeolite and zeolite/magnetite nanocomposite.

addition, the presence of the Fe₃O₄ NC caused modification in the band structure of the zeolite as seen at 663 cm⁻¹ spectra of zeolite. Also, the shift in vibrational bands of both pure zeolite and zeolite/magnetite nanocomposite confirmed the formation of both zeolite and magnetite nanoparticles.

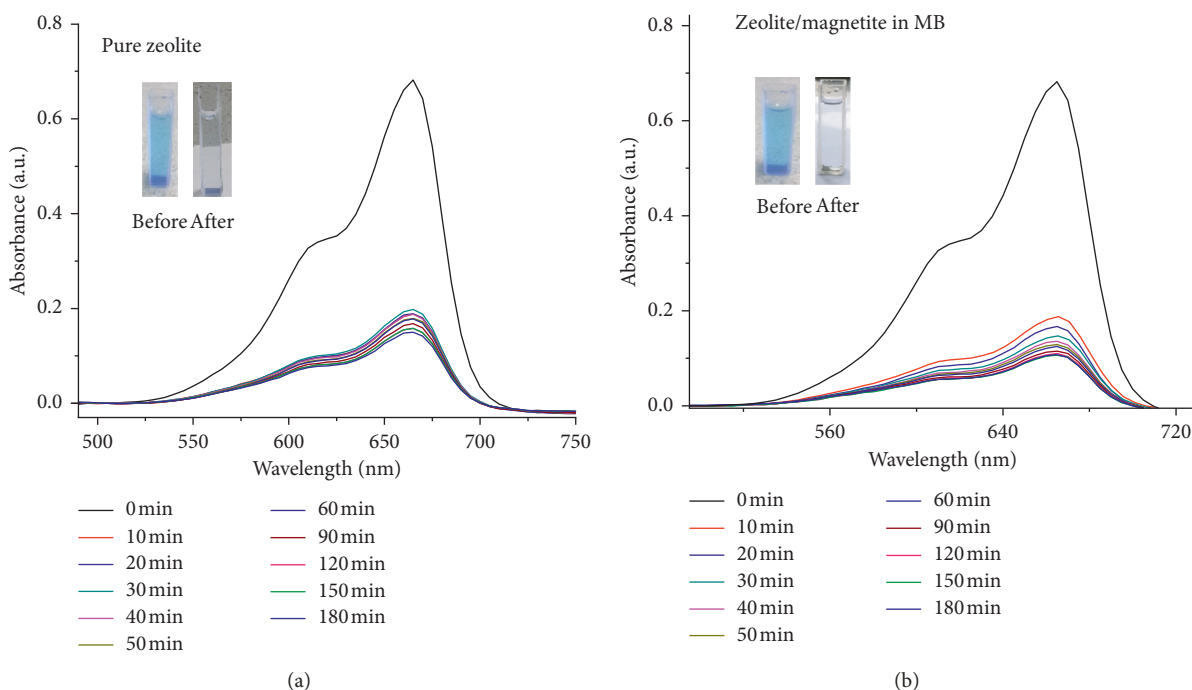


FIGURE 6: Absorbance intensity curve at various time intervals for (a) pure zeolite in MB (b) and zeolite/magnetite nanocomposite (Z-Fe₃O₄ NC) in MB.

3.5. Adsorption Studies

3.5.1. UV-Vis Equilibrium Spectra. During the adsorption studies, the feasibility of the Z-Fe₃O₄ NC adsorbent in adsorbing the MB adsorbate molecules was investigated and compared to that of pure zeolite. The results are presented in Figure 6. Generally, the graphs show that the amount of dye molecules adsorbed increased with contact time for both pure zeolite and Z-Fe₃O₄ NC adsorbent. It was also observed that the rate of adsorption decreased after first 10 minutes indicating that the availability of active sites for the dye molecules to occupy had been reduced. Thus, there was a high concentration gradient between the MB molecules and the Z-Fe₃O₄ NC within this time frame. The uptake of the MB dye molecules by the pure zeolite resulted from the highly electrostatic attraction between the cationic MB molecule and the negatively surface-charged zeolite [55]. Moussavi et al. reported that, above the p*H*_{zpc} of zeolite (p*H*_{zpc} = 7.8), the zeolite surface is negatively charged [56]; that is at the p*H* of the MB used for this study, the zeolite possessed a negatively charged surface. This allowed for the electrostatic interaction between the cationic MB and the negatively charged zeolite surface.

Moreover, after 180 minutes, Z-Fe₃O₄ NC showed higher efficiency in dye uptake of MB molecules. The presence of the magnetite nanoparticles increased the adsorption efficiency of the zeolite. Erdemoğlu and Sarıkaya reported that Fe₃O₄ at a p*H* above 5 possesses a negatively charged surface [57]. The presence of the magnetite nanoparticles in the adsorbate medium at a p*H* of 9 caused the Fe₃O₄ NC to possess negative surface charges which enhanced the adsorption by providing

TABLE 1: Removal efficiency of pure zeolite and Z-Fe₃O₄ NC

Sample	Concentration		Removal efficiency (%)
	Initial	After	
Pure zeolite	3.3624	0.3165	91
Z-Fe ₃ O ₄ NC	3.3624	0.0842	97.5

additional active sites for the adsorption of the cationic molecules of MB.

The absorbance and concentration are related through the Beer-Lambert law by a linear equation. The corresponding concentration of the absorbance values has been extracted from an established calibration curve and is tabulated in Table 1.

3.5.2. Effect of Initial Dye Concentration on Equilibrium (*q_t*).

The effect of initial dye concentration on equilibrium was conducted at 25°C by loading 2.8 mg of the Z-Fe₃O₄ NC in 3.5 mL of 2, 4, 6, 8, and 10 mg/L MB concentrations at p*H* 9 (Figure 7). The graph showed that the amount of MB dye molecules adsorbed onto the Z-Fe₃O₄ NC adsorbent increases with an increasing initial concentration of MB and increasing contact time. The increment in the dye concentration caused an increase in the driving force (concentration gradient), triggering a transfer of the MB molecules from the aqueous medium onto the surface of the adsorbent [56]. The adsorption capacity increased from 0.56–1.15 mg/g as equilibrium was reached.

3.6. Kinetic Study. The adsorption mechanism of the MB by the zeolite composite was further investigated. The data from

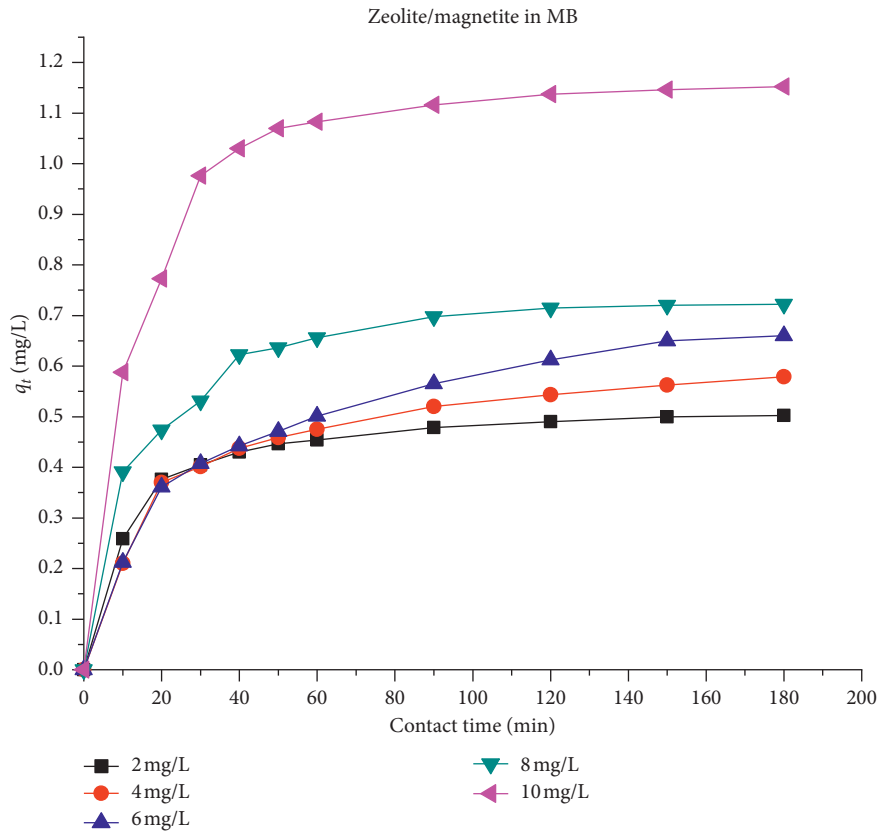
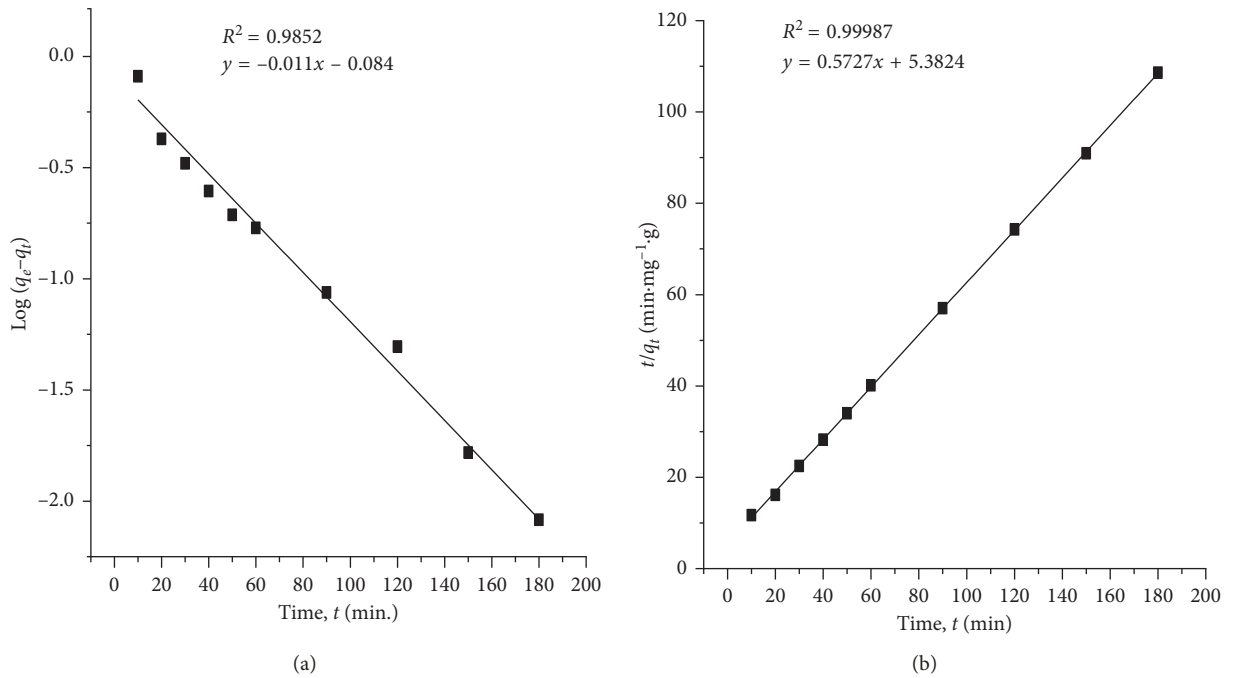
FIGURE 7: Effect of initial dye concentration on equilibrium (q_t).

FIGURE 8: Continued.

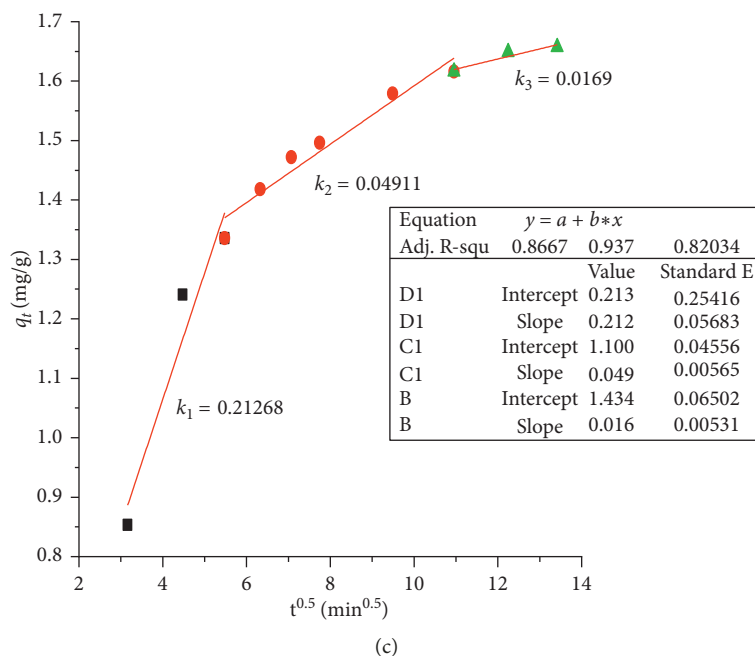


FIGURE 8: Plot of the (a) pseudo-first-order model, (b) pseudo-second-order model, and (c) intraparticle diffusion model.

the adsorption kinetics were fitted using the three kinetic models: the pseudo-first-order (PFO), pseudo-second-order (PSO), and intraparticle diffusion kinetic models. The results from these analyses are shown in Figures 8(a)–8(c). From the graph, the data fitted well with the PSO model as compared to the PFO model with correlation coefficient values of $R^2 = 0.99987$ and $R^2 = 0.98528$, respectively. The calculated $q_e = 1.6575$ mg/g from the experiment was closer to that obtained from the PSO kinetics model with a maximum adsorption capacity of 1.74587 mg/g as compared to that of the PFO (0.8224 mg/g). The R^2 and q_e values indicated that the adsorption process fitted well with the PSO.

Also, the fast-kinetic adsorption of MB in the first 10 minutes followed by a gradual adsorption can be seen from the rate constant from both the PFO and PSO. The PFO and PSO rate constants are $k_1 = 0.025333 \text{ min}^{-1}$ and $k_2 = 0.06095 \text{ min}^{0.5} \cdot \text{mg}^{-1} \cdot \text{g}$ (Table 2), respectively, indicating that the faster rate of adsorption is more directed towards that of the PSO. Thus, the PSO model describes the adsorption kinetics of the MB unto the zeolite/magnetite adsorbent as that of a chemisorption process [38, 39, 58, 59]. This confirms that the cationic MB interacted with the negatively charged zeolite.

The plot for the intraparticle diffusion model gives information on the diffusion rate parameters. From the intraparticle diffusion kinetic model, it was observed that three different intraparticle diffusion rate constants for the stepwise adsorption process influenced the rate-determining steps, as shown in Figure 8(c). The rate diffusion constant for the first linearized portion of the curve gives the highest slope ($k_1 = 0.21268 \text{ min}^{0.5} \cdot \text{mg}^{-1} \cdot \text{g}$) with a very steep gradient. At the initial stage of adsorption, there were vacant and unoccupied number of active sites for adsorption. The high concentration gradient between the adsorbate and the

TABLE 2: Parameters of kinetic models of MB adsorption on the adsorbent.

Kinetic models		
From experiment		1.6575
Calculated q_e (mg/g)		
Pseudo-first-order model		
k_1 (min^{-1})		0.025333
q_e (mg/g)		0.8224
R^2		0.98528
Pseudo-second-order model		
k_2 ($\text{g} \cdot \text{mg}^{-1} \cdot \text{min}$)		0.06095
q_e (mg/g)		1.74587
R^2		0.99987
Intraparticle diffusion model		
k_1 ($\text{g} \cdot \text{mg}^{-1} \cdot \text{min}$)		0.21268
k_2 ($\text{g} \cdot \text{mg}^{-1} \cdot \text{min}$)		0.04911
k_3 ($\text{g} \cdot \text{mg}^{-1} \cdot \text{min}$)		0.01690

adsorbent caused a high electrostatic attraction between the cationic methylene blue (MB) molecules and negative surface charge of the zeolite/magnetite adsorbent. Also, the presence of unoccupied pores in the adsorbent led to a fast-kinetic pore or surface diffusion. The second part of the model with a slope $k_2 = 0.04911 \text{ min}^{0.5} \cdot \text{mg}^{-1} \cdot \text{g}$ gives a less steep slope indicating more active sites were occupied with a limited number of unoccupied sites present. Also, the MB dye molecules were gradually diffusing into the inner pores of the adsorbent as the concentration gradient reduced gradually. The last part of the intraparticle diffusion model gives a slope, $k_3 = 0.0169 \text{ min}^{0.5} \cdot \text{mg}^{-1} \cdot \text{g}$, which is the least of the three slopes. This portion of the model describes the equilibrium state of the adsorption process. This is because, with time, the concentration gradient decreases as more active sites on the adsorbent were occupied. In addition, the

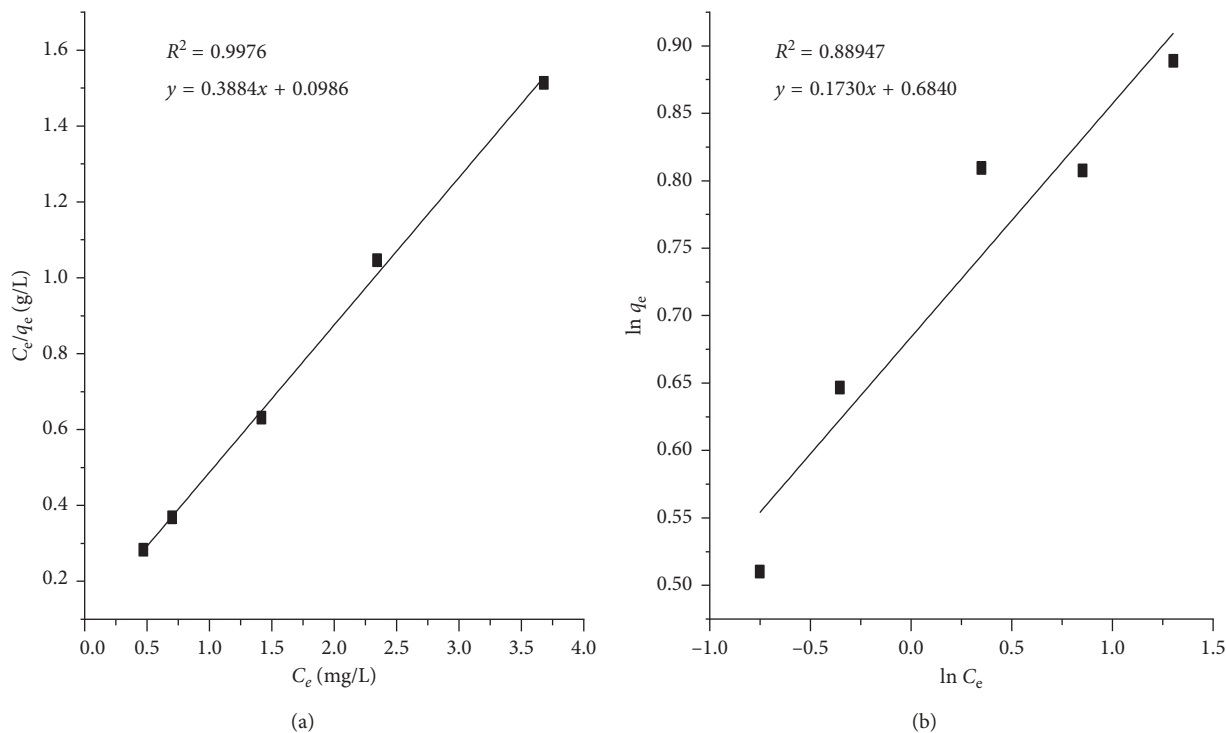


FIGURE 9: Graph of (a) Langmuir isotherm model and (b) Freundlich isotherm model.

free path for the MB molecules in the pore structure becomes narrower, and the molecules passing through become gradually blocked until equilibrium is reached where there is little or no adsorption to take place [40].

3.6.1. Sorption Isotherm Study. The equilibrium adsorption data were used to further study the adsorption isotherm of the system, by fitting it to the Langmuir and the Freundlich isotherm models, as shown in Figures 9(a) and 9(b), respectively.

From the analyses, the data fitted well with the Langmuir isotherm model having a correlation coefficient (R^2) of 0.9976 as compared to the Freundlich isotherm model with a low R^2 of 0.88947. This suggests that the Langmuir isotherm model best described the adsorption process due to its higher R^2 value indicating that the surface of the adsorbent was homogeneously covered by a monolayer of MB molecules as a result of the evenly distributed active adsorption sites present on the surface of the adsorbent. This adsorbent possesses an identical adsorption activity which allows only one dye molecule to be adsorbed per active adsorption site [56]. The maximum adsorption capacity (Q_m) was estimated to be 2.57 mg/g, indicating a homogenous monolayer saturation coverage of MB at equilibrium. The separation factor R_L obtained using the initial dye concentration lied within $0 < R_L < 1$ (i.e., 0.13369, 0.084064, 0.055558, 0.047709, and 0.036084 for the different MB concentrations) indicating a favorable adsorption of MB by the Z-Fe₃O₄ nanoadsorbent [42, 43]. The calculated parameters from the equilibrium isotherm models are presented in Table 3.

TABLE 3: Adsorption isotherm parameters.

Langmuir isotherm model	
Q_m (mg/g)	2.57407
K_L (L/mg)	0.39377
R^2	0.99760
Freundlich isotherm model	
K_F	1.98180
$1/n_f$	5.78030
R^2	0.88947

3.7. Regeneration Studies. To study the regeneration and reusability of the as-synthesized zeolite/magnetite nanocomposite, a regeneration experiment was carried out on the spent adsorbent. Among the several factors such as pH, temperature, and adsorbent type that affect the reusability of a catalyst, pH has been found to play a significant role affecting the efficiency of the spent catalyst. pH has shown to have an influential effect on the adsorption and desorption process of dye molecules due to its ability to ionize the dye molecules and to alter the surface charge characteristics and binding sites of the adsorbent [36, 60]. Desorption of MB molecules from an adsorbent in an alkaline medium is as a result of the excess OH⁻ reacting with the cationic sites of the MB molecules in solution [61, 62].

In this work, the adsorption process was conducted at a room temperature of 25°C with the same adsorbent type (Z-Fe₃O₄) and a fixed adsorbate methylene blue (MB) concentration of 2 mg/L while varying the pH parameter. During the process, the Z-Fe₃O₄ after initial loading with the dye molecules was treated with varying pH of 5, 7, 9, 11, and 13 to remove the adsorbed dye on the adsorbent. After this, the regenerated adsorbent was reloaded with

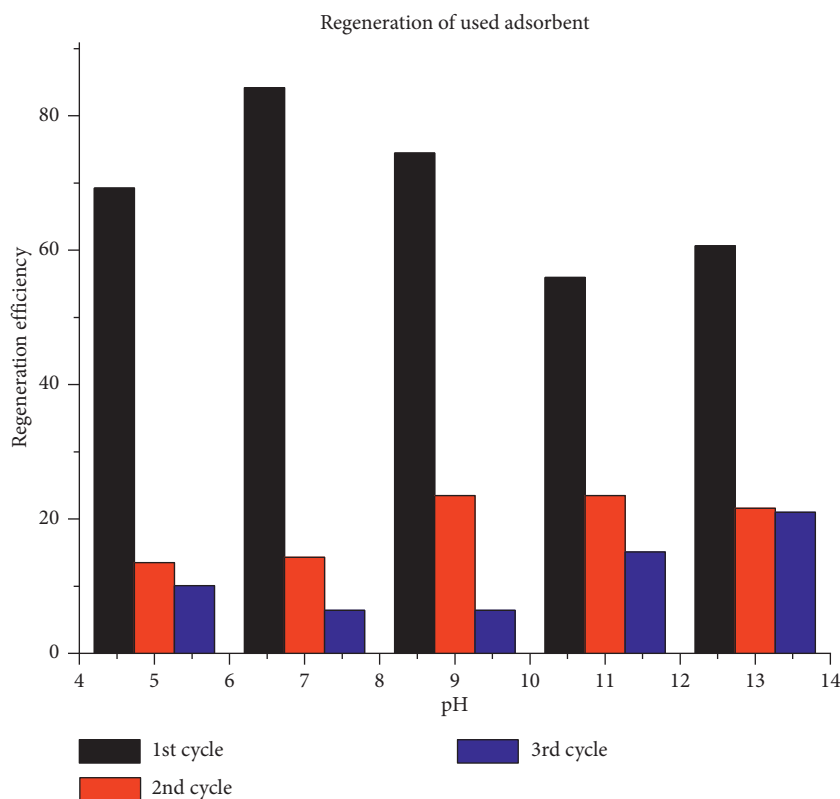


FIGURE 10: Regeneration performance of the treated zeolite/magnetite adsorbent.

the MB adsorbate and their removal efficiencies were calculated. From the results shown in Figure 10, it was observed that the spent adsorbent treated with a pH of 7 had the highest removal regeneration efficiency in the first regeneration cycle.

4. Conclusion

The magnetic zeolite/magnetite nanocomposite (Z-Fe₃O₄ NC) was successfully synthesized and used as a potential adsorbent for dye removal. Z-Fe₃O₄ NC exhibited a high adsorption capacity and high regeneration capacity after two cycles using pH 7. The adsorption of MB dye molecules onto the nanoadsorbent was controlled by the pseudo-second-order indicating that the adsorption process was that of chemisorption. The rate-controlling steps describing the adsorption process was controlled by pore, surface, and intraparticle diffusion. The Langmuir isotherm model also indicated homogeneous monolayer coverage of MB on the surface of the adsorbent during the adsorption process. The adsorption efficiency after 3 hours was 97.5%. After treating the spent adsorbent with varying pH of 5–11, the highest regeneration efficiency was achieved at a pH of 7 after three cycles. The results underscore the feasibility of Z-Fe₃O₄ NC as an adsorbent. Further work is however required to improve its regeneration capacity.

Data Availability

The data used to support the findings of this study are included within the article.

Conflicts of Interest

The authors declare that they have no conflicts of interest.

Acknowledgments

This work was supported through the University of Ghana UGRF10 research grant, the Commonwealth Early Academic Fellowship, the Cambridge-Africa Partnership for Research Excellence (CAPREx) Fellowship Programs, and the Cambridge Africa ABORADA Research Fund.

References

- [1] T. Robinson, G. McMullan, R. Marchant, and P. Nigam, "Remediation of dyes in textile effluent: a critical review on current treatment technologies with a proposed alternative," *Bioresource Technology*, vol. 77, no. 3, pp. 247–255, 2001.
- [2] E. Forgacs, T. Cserháti, and G. Oros, "Removal of synthetic dyes from wastewaters: a review," *Environment International*, vol. 30, no. 7, pp. 953–971, 2004.
- [3] M. Rafatullah, O. Sulaiman, R. Hashim, and A. Ahmad, "Adsorption of methylene blue on low-cost adsorbents: a review," *Journal of Hazardous Materials*, vol. 177, no. 1–3, pp. 70–80, 2010.
- [4] K. Rida, S. Bouraoui, and S. Hadnine, "Adsorption of methylene blue from aqueous solution by kaolin and zeolite," *Applied Clay Science*, vol. 83–84, pp. 99–105, 2013.
- [5] G. Z. Kyzas and K. A. Matis, "Nanoadsorbents for pollutants removal: a review," *Journal of Molecular Liquids*, vol. 203, pp. 159–168, 2015.
- [6] C. Santhosh, V. Velmurugan, G. Jacob, S. K. Jeong, A. N. Grace, and A. Bhatnagar, "Role of nanomaterials in

- water treatment applications: a review," *Chemical Engineering Journal*, vol. 306, pp. 1116–1137, 2016.
- [7] Z. Bai, B. Sun, N. Fan et al., "Branched mesoporous Mn_3O_4 nanorods: facile synthesis and catalysis in the degradation of methylene blue," *Chemistry—A European Journal*, vol. 18, no. 17, pp. 5319–5324, 2012.
- [8] U. Pal, A. Sandoval, S. I. U. Madrid, G. Corro, V. Sharma, and P. Mohanty, "Mixed titanium, silicon, and aluminum oxide nanostructures as novel adsorbent for removal of rhodamine 6G and methylene blue as cationic dyes from aqueous solution," *Chemosphere*, vol. 163, pp. 142–152, 2016.
- [9] D. Dodoo-Arhin, F. P. Buabeng, J. M. Mwabora et al., "The effect of titanium dioxide synthesis technique and its photocatalytic degradation of organic dye pollutants," *Heliyon*, vol. 4, no. 7, article e00681, 2018.
- [10] S. Recillas, J. Colón, E. Casals et al., "Chromium VI adsorption on cerium oxide nanoparticles and morphology changes during the process," *Journal of Hazardous Materials*, vol. 184, no. 1–3, pp. 425–431, 2010.
- [11] L. Chai, Y. Wang, N. Zhao, W. Yang, and X. You, "Sulfate-doped $\text{Fe}_3\text{O}_4/\text{Al}_2\text{O}_3$ nanoparticles as a novel adsorbent for fluoride removal from drinking water," *Water Research*, vol. 47, no. 12, pp. 4040–4049, 2013.
- [12] H. M. Cui, H. Liu, J. Y. Wang, X. Li, and F. Han, "Agglomeration and dispersion of nano-scale powders," *Materials for Mechanical Engineering (China)*, vol. 28, no. 8, pp. 38–41, 2004.
- [13] S. Debnath and U. C. Ghosh, "Equilibrium modeling of single and binary adsorption of Cd (II) and Cu (II) onto agglomerated nano structured titanium (IV) oxide," *Desalination*, vol. 273, no. 2-3, pp. 330–342, 2011.
- [14] A. Mikolajczyk, A. Gajewicz, B. Rasulev et al., "Zeta potential for metal oxide nanoparticles: a predictive model developed by a nano-quantitative structure-property relationship approach," *Chemistry of Materials*, vol. 27, no. 7, pp. 2400–2407, 2015.
- [15] R. J. White, R. Luque, V. L. Budarin, J. H. Clark, and D. J. Macquarrie, "Supported metal nanoparticles on porous materials. Methods and applications," *Chemical Society Reviews*, vol. 38, no. 2, pp. 481–494, 2009.
- [16] M. E. Davis, "Ordered porous materials for emerging applications," *Nature*, vol. 417, no. 6891, pp. 813–821, 2002.
- [17] Q. Yin, X. Qi, M. A. Biberger, and D. Leamon: U.S. Patent Application No. 12/962,518, 2011.
- [18] J. Otsu and Y. Oshima, "New approaches to the preparation of metal or metal oxide particles on the surface of porous materials using supercritical water: development of supercritical water impregnation method," *The Journal of Supercritical Fluids*, vol. 33, no. 1, pp. 61–67, 2005.
- [19] M.-H. Liao and D.-H. Chen, "Preparation and characterization of a novel magnetic nano-adsorbent," *Journal of Materials Chemistry*, vol. 12, no. 12, pp. 3654–3659, 2002.
- [20] J. Gómez-Pastora, E. Bringas, and I. Ortiz, "Recent progress and future challenges on the use of high performance magnetic nano-adsorbents in environmental applications," *Chemical Engineering Journal*, vol. 256, pp. 187–204, 2014.
- [21] S.-H. Huang and D.-H. Chen, "Rapid removal of heavy metal cations and anions from aqueous solutions by an amino-functionalized magnetic nano-adsorbent," *Journal of Hazardous Materials*, vol. 163, no. 1, pp. 174–179, 2009.
- [22] R. M. Cornell and U. Schwertmann, *The Iron Oxides: Structure, Properties, Reactions, Occurrences and Uses*, John Wiley & Sons, Hoboken, NJ, USA, 2003.
- [23] V. Jassal, U. Shanker, and S. Gahlot, "Green synthesis of some iron oxide nanoparticles and their interaction with 2-amino, 3-amino and 4-aminopyridines," *Materials Today: Proceedings*, vol. 3, no. 6, pp. 1874–1882, 2016.
- [24] H. Jiao and H. Yang, "Controlled synthesis and magnetic properties of Fe_3O_4 walnut spherical particles and octahedral microcrystals," *Science in China Series E: Technological Sciences*, vol. 51, no. 11, pp. 1911–1920, 2008.
- [25] J. H. Wu, S. P. Ko, H. L. Liu et al., "Sub 5 nm Fe_3O_4 nanocrystals via coprecipitation method," *Colloids and Surfaces A: Physicochemical and Engineering Aspects*, vol. 313–314, pp. 268–272, 2008.
- [26] M. N. Islam, L. V. Phong, J. R. Jeong, and C. Kim, "A facile route to sonochemical synthesis of magnetic iron oxide (Fe_3O_4) nanoparticles," *Thin Solid Films*, vol. 519, no. 23, pp. 8277–8279, 2011.
- [27] A. B. Seabra, P. Haddad, and N. Duran, "Biogenic synthesis of nanostructured iron compounds: applications and perspectives," *IET Nanobiotechnology*, vol. 7, no. 3, pp. 90–99, 2013.
- [28] Z. Izadiyan, K. Shameli, M. Miyake et al., "Cytotoxicity assay of plant-mediated synthesized iron oxide nanoparticles using Juglans regia green husk extract," *Arabian Journal of Chemistry*, 2018, In press.
- [29] A. L. Daniel-da-Silva, T. Trindade, B. J. Goodfellow, B. F. O. Costa, R. N. Correia, and A. M. Gil, "In situ synthesis of magnetite nanoparticles in carrageenan gels," *Biomacromolecules*, vol. 8, no. 8, pp. 2350–2357, 2007.
- [30] P. Mohanpuria, N. K. Rana, and S. K. Yadav, "Biosynthesis of nanoparticles: technological concepts and future applications," *Journal of Nanoparticle Research*, vol. 10, no. 3, pp. 507–517, 2008.
- [31] I. Petrov and T. Michalev, "Synthesis of zeolite A: a review," 2012.
- [32] E. Nyankson, J. K. Efavi, A. Yaya et al., "Synthesis and characterisation of zeolite-A and Zn-exchanged zeolite-A based on natural aluminosilicates and their potential applications," *Cogent Engineering*, vol. 5, no. 1, p. 1440480, 2018.
- [33] E. Koohsaryan and M. Anbia, "Nanosized and hierarchical zeolites: a short review," *Chinese Journal of Catalysis*, vol. 37, no. 4, pp. 447–467, 2016.
- [34] H. C. Junqueira, D. Severino, L. G. Dias, M. S. Gugliotti, and M. S. Baptista, "Modulation of methylene blue photochemical properties based on adsorption at aqueous micelle interfaces," *Physical Chemistry Chemical Physics*, vol. 4, no. 11, pp. 2320–2328, 2002.
- [35] M. Doğan, M. Alkan, A. Türkyilmaz, and Y. Özdemir, "Kinetics and mechanism of removal of methylene blue by adsorption onto perlite," *Journal of Hazardous Materials*, vol. 109, no. 1–3, pp. 141–148, 2004.
- [36] Y. Li, Q. Du, T. Liu et al., "Methylene blue adsorption on graphene oxide/calcium alginate composites," *Carbohydrate Polymers*, vol. 95, no. 1, pp. 501–507, 2013.
- [37] S. Lagergren, "Zur theorie der sogenannten adsorption gelöster stoffe," *Zeitschrift für Chemie und Industrie der Kolloide*, vol. 2, no. 1, pp. 1–39, 1898.
- [38] H. Qiu, L. Lv, B.-C. Pan, Q.-J. Zhang, W.-M. Zhang, and Q.-X. Zhang, "Critical review in adsorption kinetic models," *Journal of Zhejiang University-SCIENCE A*, vol. 10, no. 5, pp. 716–724, 2009.
- [39] Y. S. Ho and G. McKay, "Pseudo-second order model for sorption processes," *Process Biochemistry*, vol. 34, no. 5, pp. 451–465, 1999.
- [40] W. J. Weber and J. C. Morris, "Kinetics of adsorption on carbon from solution," *Journal of the Sanitary Engineering Division*, vol. 89, no. 2, pp. 31–60, 1963.

- [41] P. Somasundaran, *Encyclopedia of Surface and Colloid Science*, Taylor & Francis, New York, NY, USA, 2nd edition, 2006.
- [42] I. Langmuir, "The adsorption of gases on plane surfaces of glass, mica and platinum," *Journal of the American Chemical Society*, vol. 40, no. 9, pp. 1361–1403, 1918.
- [43] G. Vijayakumar, R. Tamilarasan, and M. Dharmendirakumar, "Adsorption, kinetic, equilibrium and thermodynamic studies on the removal of basic dye rhodamine-B from aqueous solution by the use of natural adsorbent perlite," *Journal of Materials and Environmental Science*, vol. 3, no. 1, pp. 157–170, 2012.
- [44] L. Vafajoo, F. Ghanaat, and A. Ghalebi, "An investigation of a petrochemical wastewater treatment utilizing GAC: a study of adsorption kinetics," *APCBEE Procedia*, vol. 10, pp. 131–135, 2014.
- [45] C. Yan, C. Wang, J. Yao, L. Zhang, and X. Liu, "Adsorption of methylene blue on mesoporous carbons prepared using acid- and alkaline-treated zeolite X as the template," *Colloids and Surfaces A: Physicochemical and Engineering Aspects*, vol. 333, no. 1–3, pp. 115–119, 2009.
- [46] H. Freundlich, "Über die adsorption in lösungen," *Journal of Physical Chemistry*, vol. 57U, no. 1, pp. 385–470, 1907.
- [47] M. M. J. Treacy and J. B. Higgins, *Collection of Simulated XRD Powder Patterns for Zeolites*, Elsevier on Behalf of the Structure Commission of the International Zeolite Association, Amsterdam, Netherlands, 2001.
- [48] Y. Cai, Y. Shen, A. Xie, S. Li, and X. Wang, "Green synthesis of soya bean sprouts-mediated superparamagnetic Fe_3O_4 nanoparticles," *Journal of Magnetism and Magnetic Materials*, vol. 322, no. 19, pp. 2938–2943, 2010.
- [49] T. Mohammadi and A. Pak, "Making zeolite A membrane from kaolin by electrophoresis," *Microporous and Mesoporous Materials*, vol. 56, no. 1, pp. 81–88, 2002.
- [50] P. Chutia, S. Kato, T. Kojima, and S. Satokawa, "Arsenic adsorption from aqueous solution on synthetic zeolites," *Journal of Hazardous Materials*, vol. 162, no. 1, pp. 440–447, 2009.
- [51] T. M. Salem Attia, X. L. Hu, and D. Q. Yin, "Synthesised magnetic nanoparticles coated zeolite (MNCZ) for the removal of arsenic (As) from aqueous solution," *Journal of Experimental Nanoscience*, vol. 9, no. 6, pp. 551–560, 2014.
- [52] M. Gougazeh and J.-C. Buhl, "Synthesis and characterization of zeolite A by hydrothermal transformation of natural Jordanian kaolin," *Journal of the Association of Arab Universities for Basic and Applied Sciences*, vol. 15, no. 1, pp. 35–42, 2014.
- [53] S. V. Stefanovsky, O. I. Stefanovskaya, S. E. Vinokurov, S. S. Danilov, and B. F. Myasoedov, "Phase composition, structure, and hydrolytic durability of glasses in the $\text{Na}_2\text{O}-\text{Al}_2\text{O}_3-(\text{Fe}_2\text{O}_3)-\text{P}_2\text{O}_5$ system at replacement of Al_2O_3 by Fe_2O_3 ," *Radiochemistry*, vol. 57, no. 4, pp. 348–355, 2015.
- [54] B. Tanhaei, A. Ayati, M. Lahtinen, and M. Sillanpää, "Preparation and characterization of a novel chitosan/ Al_2O_3 /magnetite nanoparticles composite adsorbent for kinetic, thermodynamic and isotherm studies of methyl orange adsorption," *Chemical Engineering Journal*, vol. 259, pp. 1–10, 2015.
- [55] C. Li, H. Zhong, S. Wang, J. Xue, and Z. Zhang, "Removal of basic dye (methylene blue) from aqueous solution using zeolite synthesized from electrolytic manganese residue," *Journal of Industrial and Engineering Chemistry*, vol. 23, pp. 344–352, 2015.
- [56] G. Moussavi, S. Talebi, M. Farrokhi, and R. M. Sabouti, "The investigation of mechanism, kinetic and isotherm of ammonia and humic acid co-adsorption onto natural zeolite," *Chemical Engineering Journal*, vol. 171, no. 3, pp. 1159–1169, 2011.
- [57] M. Erdemoğlu and M. Sarıkaya, "Effects of heavy metals and oxalate on the zeta potential of magnetite," *Journal of Colloid and Interface Science*, vol. 300, no. 2, pp. 795–804, 2006.
- [58] B. H. Hameed, A. L. Ahmad, and K. N. A. Latiff, "Adsorption of basic dye (methylene blue) onto activated carbon prepared from rattan sawdust," *Dyes and Pigments*, vol. 75, no. 1, pp. 143–149, 2007.
- [59] R. Han, J. Zhang, P. Han, Y. Wang, Z. Zhao, and M. Tang, "Study of equilibrium, kinetic and thermodynamic parameters about methylene blue adsorption onto natural zeolite," *Chemical Engineering Journal*, vol. 145, no. 3, pp. 496–504, 2009.
- [60] R. Lafi, I. Montasser, and A. Hafiane, "Adsorption of Congo red dye from aqueous solutions by prepared activated carbon with oxygen-containing functional groups and its regeneration," *Adsorption Science & Technology*, vol. 37, no. 1–2, pp. 160–181, 2019.
- [61] B. A. Fil, C. Ozmetin, and M. Korkmaz, "Cationic dye (methylene blue) removal from aqueous solution by montmorillonite," *Bulletin of the Korean Chemical Society*, vol. 33, no. 10, pp. 3184–3190, 2012.
- [62] H. Zhang, X. Li, G. He, J. Zhan, and D. Liu, "Preparation of magnetic composite hollow microsphere and its adsorption capacity for basic dyes," *Industrial & Engineering Chemistry Research*, vol. 52, no. 47, pp. 16902–16910, 2013.



Hindawi

Submit your manuscripts at
www.hindawi.com

